

We are IntechOpen, the world's leading publisher of Open Access books Built by scientists, for scientists

6,900

Open access books available

186,000

International authors and editors

200M

Downloads

Our authors are among the

154

Countries delivered to

TOP 1%

most cited scientists

12.2%

Contributors from top 500 universities



WEB OF SCIENCE™

Selection of our books indexed in the Book Citation Index
in Web of Science™ Core Collection (BKCI)

Interested in publishing with us?
Contact book.department@intechopen.com

Numbers displayed above are based on latest data collected.
For more information visit www.intechopen.com



Photothermal Techniques in Material Characterization

Marios Nestoros

Additional information is available at the end of the chapter

<http://dx.doi.org/10.5772/56039>

1. Introduction

The 21st century is characterized by a rapid increase in technological applications which involve the design and development of materials with tailored properties that manifest and take advantage of scientific developments from the region of modern physics. In medicine and biology there is a need of new materials that are biocompatible and exhibit similar biological behavior to that of several types of human tissue. In structural engineering there are new approaches for the production of concrete materials that can withstand tension, can self-repair and self-monitor structural damage. Organic semiconductors and devices based on nanomaterials unfold new dimensions in optoelectronics, information technology and renewable energy applications.

The field of photothermal physics and the related characterization techniques is becoming increasingly important with the advance in the design and production of “new materials” (composite materials/heterostructures). Several photothermal techniques present significant advantages over traditional material characterization techniques, mainly due to their non-contact and non-destructive nature. Photothermal techniques offer high sensitivity relative to the thermal and optoelectronic properties of materials although in most cases the extraction of the aforementioned parameters is not direct and involves much computational effort. In addition in several cases the above techniques can be used to monitor in real time industrial or in-lab processes.

In this chapter the concept of thermal and electronic wave methodology will be initially introduced, followed by information on a brief description of experimental setups and recent advances in the field. The chapter will focus on the presentation of examples from the application of some photothermal techniques in the characterization of composite materials and thin metal films used as gas sensors.

2. Thermal and electronic waves

The optical absorption of an intensity modulated beam of light results in the diffusion of the generated heat through the sample according to Fourier's law. Due to the periodic nature of the excitations, one expects a periodic temperature response. The combination of Fourier's Law and energy conservation provides the conduction heat transfer equation [1]:

$$\nabla^2 T(r, t) - \frac{1}{D_T} \frac{\partial}{\partial t} T(r, t) = -\frac{1}{\kappa} Q(r, t) \quad (1)$$

In the above equation the temperature T is a function of position r and time t . The temperature depends on the thermal diffusivity D_T and on the thermal conductivity κ of the material. The heat source term $Q(r, t)$ is measured in $W \cdot m^{-3}$ and is modulated at an angular frequency $\omega = 2\pi f$. In the case of one dimensional heat flux along the z axis the heat source term takes the form

$$Q(x, t) = \frac{1}{2} \cdot I_0 \cdot (1 - R) \cdot \alpha \cdot e^{-\alpha \cdot z} (1 + e^{i \cdot \omega \cdot t}) \quad (2)$$

Assuming one dimensional heat flow along z direction, introducing eq.(2) into eq.(1) and taking the temporal Fourier transform of eq.(1) one gets the following differential equation for the ac temperature field ΔT in the material

$$\frac{d^2 \Delta T(z, \omega)}{dz^2} - \sigma_T^2(\omega) \Delta T(\omega) = -\frac{\alpha \cdot I_0 \cdot (1 - R)}{k} e^{-\alpha \cdot z} \quad (3)$$

In the above equations α and R , are respectively the optical absorption coefficient and reflectivity at the excitation wavelength and I_0 is the incident optical intensity (in W/m^2).

A fundamental quantity for the thermal waves [1] which are the solutions of eq.(3) is the thermal wavenumber σ_T [1] defined as:

$$\sigma_T = \sqrt{\frac{i\omega}{D}} = (1+i) \sqrt{\frac{\omega}{2D}} \equiv \frac{(1+i)}{\mu} \quad (4)$$

The quantity μ_T is the thermal diffusion length defined as:

$$\mu_T = \sqrt{\frac{2D_T}{\omega}} = \sqrt{\frac{D_T}{\pi \cdot f}} \quad (5)$$

At high modulation frequencies (f) the thermal diffusion length μ_T is small, so the thermal waves are restricted near the surface of the sample, while at low modulation frequencies the thermal wave centroid lies deeper in the material. The ac temperature field ΔT has an amplitude and phase (relative to the excitation) that can be measured with different photothermal configurations and reveal the thermal properties of the material under investigation.

In semiconducting materials, if the incident photon energy ($h\nu$) is above the energy gap (E_g), the optical excitation results in the generation of free electron and hole populations that contribute to the conductivity of the material. On a picosecond time scale electrons and holes become thermalized with the lattice through phonon interaction, releasing the excess energy $h\nu - E_g$, and lie on the bottom of the conduction band (electrons) and top of the valence band (holes). Then, electrons and holes diffuse for some time, known as carrier lifetime τ , before they recombine through non-radiative recombination processes, giving thermal energy $h\nu$ to the lattice. Following an approach similar to the one described above for thermal waves, one can formulate an equation for the plasma (electron-hole) diffusion equation:

$$\frac{d^2 \Delta N(z, \omega)}{dz^2} - \sigma_N^2 \cdot \Delta N(z, \omega) = -\frac{I_0 \cdot (1-R)}{D_N} \alpha \cdot e^{-\alpha \cdot z} \quad (6)$$

Where ΔN is the ac component of the plasma concentration in m^{-3} , D_N is the electronic diffusivity of the material and σ_N is the electronic wave number defined as

$$\sigma_N = \sqrt{\frac{1 + i \cdot \omega \cdot \tau}{D \cdot \tau}} \quad (7)$$

The electronic diffusion length is defined as

$$\mu_N \equiv \frac{1}{\text{Re}(\sigma_N)} = \sqrt{\frac{2 \cdot D_N \cdot \tau}{1 + \sqrt{1 + \omega^2 \cdot \tau^2}}} \quad (8)$$

At high modulation frequencies $\omega\tau \gg 1$ the expression for the electronic diffusion length takes a similar form to that for the thermal diffusion length and depends on the modulation frequency, $\mu_N = (D_N/\pi f)^{1/2}$. At small modulation frequencies the electronic diffusion length is constant, $\mu_N = (D_N \cdot \tau)^{1/2}$, and the plasma wave is in phase with the optical excitation.

The dimensionality of the diffusion problem (thermal/plasma) depends on the relation of the diffusion length (thermal, electronic) to the spot sizes of the pump beam and the probe beam. The assumption of one dimensional propagation for the thermal/electronic wave is a valid as long as the thermal/electronic diffusion length is smaller than the spot size of the beam.

Here we have to mention that in the case of semiconductors the heat source [2,3] included in the thermal diffusion equation has to be modified in order to include the heat released by the

thermalization of free carriers which is proportional to $h\nu - E_g$ as well as the one due to non-radiative recombination which is proportional to E_g/τ . Hence the thermal diffusion equation takes the form

$$\frac{d^2\Delta T(z, \omega)}{dz^2} + \frac{E_g}{\kappa \cdot \tau} \Delta N(z, \omega) - \sigma_T^2 \cdot \Delta T(z, \omega) = -\frac{(h\nu - E_g) \cdot \alpha \cdot I_0 \cdot (1 - R) \cdot e^{-\alpha \cdot z}}{\kappa \cdot h\nu} \quad (9)$$

This means that the system of thermal and plasma diffusion equations is coupled and one should first seek the solution of the plasma equation and then the thermal one.

The appropriate boundary conditions [2,3] have to be applied depending on the sample structure (two layer, multilayer) in order to get the solutions of the ac fields $\Delta T(z, \omega)$ and $\Delta N(z, \omega)$. The boundary conditions involve the continuity of heat flux and temperature at the interfaces, as well as the continuity of carrier concentration at the interfaces and the recombination of free carriers at the surfaces and interfaces.

3. Instrumentation and setup of some photothermal techniques

3.1. Photomodulated Thermoreflectance (PMTR)

Photomodulated Thermoreflectance (PMTR) has been used extensively for the characterization of a variety of implanted semiconductors and layered structures [3-9]. Concerning applications in electronic materials one can mention among others: ion implantation monitoring, annealing kinetics of defects [5,6], etch monitoring and carrier lifetime evaluation [6,7], thin metal film measurements [4]. The technique is based on the detection of local temperature excursions on the surface of the material under investigation induced by an intensity modulated light beam (pump) via the monitoring of the surface reflectance with the aid of another light beam (probe). The non-contact and non-destructive character of the technique in addition to the high sensitivity to thermal inhomogeneities, make PMTR an attractive material evaluation technique. The technological trend towards smaller structures in the field of microelectronics creates the need for characterization techniques with improved spatial resolution. Such a technique is PMTR-microscopy (micro PMTR) [10], a variant of PMTR which combines the advantages of the PMTR technique mentioned above, with the various functions of a microscope offering the ability of viewing the sample under test while characterizing it. In addition it offers an improved spatial resolution as compared to the conventional PMTR technique. A conventional PMTR setup (Figure 1) as the one used for the experiments described in the applications discussed in this chapter, is described below.

An Ar⁺ laser operating at the main lines of 488 nm and 514.5 nm is used as the excitation source providing the pump beam with an intensity that is modulated by an acousto-optic modulator. The pump beam (typical power 60 mW) is then focused onto the sample's surface at a nearly normal incidence to a spot size that can be varied. The reflectivity changes of the surface due to

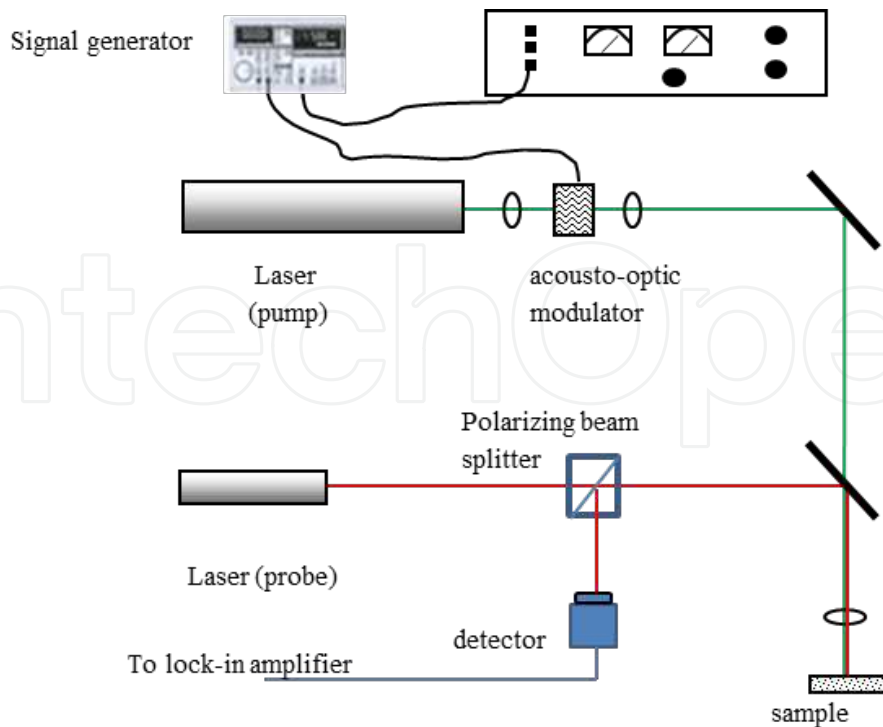


Figure 1. PMTR setup

the photo-induced thermal and or plasma waves are probed by a He–Ne Laser operating at 632.8 nm and at a power of a few mW. The probe beam is focused onto the sample collinearly to the pump beam. The reflected probe beam is diverted with the aid of a polarizing beam splitter to a silicon photodiode, filtered by a 632.8nm band pass interference filter. In order to reject any signal contributions arising from the thermoelastic deformation of the sample surface, the detector is deliberately underfilled, and is operated in the sum mode. The output of the detector is monitored with a fast lock-in amplifier, synchronous with the Ar⁺ modulation of various frequencies. The in-phase and quadrature components of the signal are stored in the computer for subsequent analysis and display. The PMTR signal S_{PMTR} is proportional to the reflectivity change ΔR of the sample's surface ($z=0$) and can be expressed as

$$S_{PMTR}(\omega) \equiv \frac{\Delta R}{R} = \frac{1}{R} \frac{\partial R}{\partial T} \cdot \Delta T(z=0, \omega) + \frac{1}{R} \frac{\partial R}{\partial N} \cdot \Delta N(z=0, \omega) \quad (10)$$

3.2. Photothermal Radiometry (PTR)

Photothermal radiometry [9-11] relies on the monitoring of modulated blackbody radiation emitted from a material that is optically excited by an intensity modulated monochromatic light beam. Following partial or total absorption of the incident radiation, a portion of it is converted into heat. The subsequent diffusion of heat is dictated by thermal transport properties like thermal diffusivity and thermal conductivity. In semiconducting samples the photoexcited carriers behave as Planck radiators that contribute to the black body emission.

In the case of good quality semiconductors the contribution of free carriers is the main component of the PTR signal which has an amplitude that is proportional to free carrier's lifetime. As a result photothermal techniques allow the determination of optical, electronic as well as thermophysical properties of materials even in cases of efficient light scattering materials, which prohibit their characterization through conventional optical techniques. Photothermal radiometry has been used to characterize a variety of materials and thin films ranging from semiconducting films [11,12,14] to nanotube/nanoparticle composites [15,16] and biomaterials [17]. The PTR experimental setup (shown in Figure 2) consists of an excitation laser source (DPSS laser emitting at 512 nm), an acousto-optic cell that chops periodically the laser intensity, an MCT (Mercury, Cadmium- Telluride) detector with detection in the 2 μm -12 μm wavelength range, a preamplifier, a phase sensitive detection system (lock in amplifier) and a couple of off axis Ag coated paraboloid mirrors to gather and collimate the black body radiation emitted from the excited sample in the sensitive detector area. The excitation beam with incident power illuminates the sample surface almost at normal incidence. As the modulation frequency is varied (typical frequency span 10^0 - 10^6 Hz) the signal amplitude and phase is recorded. In order to calculate the instrumental transfer function with which we have to correct the experimental data, a frequency scan of a thick and opaque sample (steel disc) is usually performed. The PTR signal S_{PTR} can be expressed in most of the cases as an integral of the temperature field and the plasma field (in the case of semiconductors) over the thickness of the sample multiplied by appropriate coefficients C_1 and C_2 [14].

$$S_{\text{PTR}}(\omega) = C_1 \cdot \int_0^l \Delta T(z, \omega) \cdot dz + C_2 \cdot \int_0^l \Delta N(z, \omega) \cdot dz \quad (11)$$

4. Applications of photothermal techniques in materials characterization

4.1. Analysis of Hydrogen adsorption and desorption on palladium thin films with photomodulated thermoreflectance measurements

The importance of hydrogen gas technology is growing due to the many industrial applications as well as the needs for environmentally clean energy resources. Nevertheless hydrogen gas has some disadvantages concerning its storage and its flammability. For these reasons there is a need for hydrogen sensors with high sensitivity and fast response. In addition the reaction kinetics of hydrogen gas with the surface of the sensor is quite interesting from the viewpoint of physical chemistry and materials science. In this paragraph the kinetics of hydrogen adsorption and desorption on palladium thin films was studied [18] via photomodulated thermoreflectance (PMTR) measurements. The analysis of the experimental data is based on a Langmuirian isothermal model which supports a dissociative adsorption of hydrogen on palladium followed by molecular desorption. The values of the adsorption and desorption rate constants were determined and their values are discussed. The response and recovery times

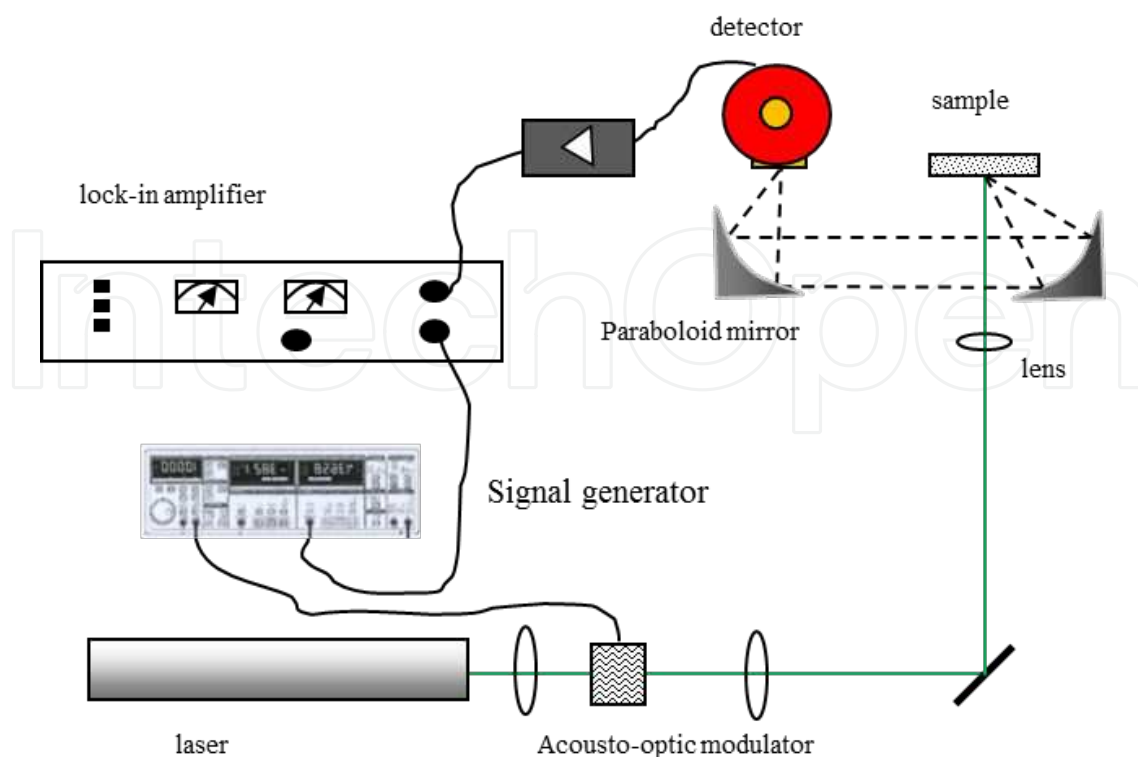


Figure 2. PTR setup

of the sensor were measured and their dependence on hydrogen concentration is also explored and discussed.

4.1.1. Sample details and experimental methodology

The sensor consists of a palladium thin film, with a thickness of 6 nm, evaporated on silicon substrate, with an intermediate layer of silicon oxide. In hydrogen atmosphere the PMTR signal from such sensors alters due to the adsorption of hydrogen onto the palladium film and the formation of the palladium hydride. The formation of the PdH_x modifies the electronic structure of the palladium metal and also changes the Pd lattice constant. These modifications finally change the refractive index and the reflectance of the Pd film surface [19,20]. The experimental setup has been discussed earlier in this chapter. The excitation beam (Ar^+ laser operating at 488 nm) power was set at 100 mW and the diameter of the spot size on the samples was 50 μm . The reflectivity changes of the surface were monitored by a He-Ne Laser operating at 632.8 nm and a power of 0.5 mW. The probe beam was focused onto the sample to a spot size of 35 μm , collinearly to the pump beam. The modulation frequency value of the pump beam was set at 1 kHz since at this frequency the signal was stable, with a good signal to noise ratio.

The thin film sensor was placed in a cylindrical cell (radius of 4.7 cm and length of 15.6 cm) with a gas input and output system as well as a temperature controller. High accuracy

flowmeters were used in order to supply hydrogen and nitrogen in the cylinder at the desired ratio and at a constant flow rate of 150 mL/min. The temperature was raised up to 100°C, and the samples were exposed to different hydrogen concentrations (from 25 to 150 ppb), in nitrogen atmosphere.

4.1.2. Reaction kinetics and the PMTR signal

The differential equations describing the adsorption process result from the kinetics of the chemical reaction and the application of the Langmuirian model [20,21].

In the case of the molecular adsorption $S^* + H_2(gas) \xrightleftharpoons[k_d]{k_a} S-H_2$ and considering that the rate constant of adsorption k_a is many orders of magnitude bigger than the rate constant of desorption k_d the time evolution of the coverage is

$$\theta_p(t) = 1 - \exp[-k_a P(t - t_0)] \quad (12)$$

The partial pressure of hydrogen H_2 is P and t_0 the time at which hydrogen is deployed to the chamber, i.e. $\theta(t_0) = 0$.

In the case of dissociative adsorption $2S^* + H_2(gas) \xrightleftharpoons[k_d]{k_a} 2S-H$ the solution of the governing differential equation is

$$\theta_p(t) = \frac{k_a P \tanh(\sqrt{k_a k_d P}(t - t_0))}{\sqrt{k_a k_d P} + k_a P \tanh(\sqrt{k_a k_d P}(t - t_0))} \quad (13)$$

After a Taylor expansion of the hyperbolic tangents around $\sqrt{k_a k_d P} \approx 0$ up to first order, the solution is

$$\theta_p(t) = \frac{k_a P(t - t_0)}{1 + k_a P(t - t_0)} \quad (14)$$

The processes of adsorption and desorption happen simultaneously and the negative sign of the desorption term shows that the two processes are competitive. The terms which describe the desorption from the Pd surface and the adsorption of hydrogen at the Pd-SiO₂ interface were not taken into account. This is because the diffusion of hydrogen adsorbed atoms and their adsorption to interface happen so rapidly, that the amount of the adsorbed hydrogen at the interface is constantly in equilibrium with that at the surface [22]. According to Lundström

et al. [22], when the hydrogen partial pressure is lower than 200 Pa, the response signal of the hydrogen sensor $\Delta\xi$ is proportional to the surface coverage θ . At a partial pressure P , the signal's time dependence is given by:

$$\Delta\xi = \alpha \theta_p(t) \tag{15}$$

Hence the PMTR signal evolution, presented in Fig. 3, is given by the equation:

$$\xi(t) = \frac{\Delta\xi_s}{\theta_s} \theta_p(t) + \xi_0 \tag{16}$$

where $\Delta\xi_s$ is the maximum change of the photothermal signal, which happens at $t \rightarrow \infty$ and is defined in Figure 3(b). It's obvious that, θ_s and $\Delta\xi_s$ are slightly larger than θ_f and $\Delta\xi_f$, because the former is defined at $t \rightarrow \infty$ while the latter is defined at t_f . In the steady state ($d\theta/dt=0$) the coverage at saturation θ_s for molecular and dissociative adsorption is given respectively by:

$$\theta_s|_{mol} = \frac{k_a P}{k_d + k_a P} \tag{a}$$

$$\theta_s|_{diss} = \frac{\sqrt{k_a P}}{\sqrt{k_d} + \sqrt{k_a P}} \tag{b}$$
(17)

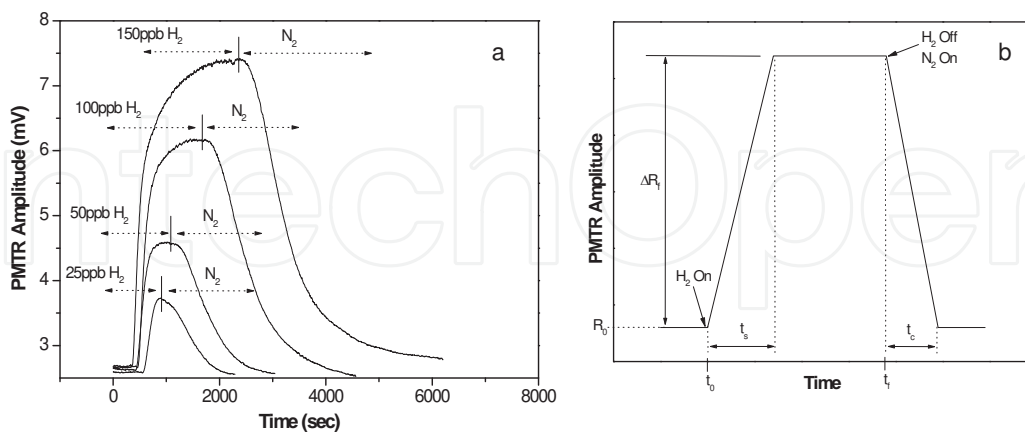


Figure 3. (a) PMTR signal response during adsorption and desorption of different H₂ concentrations, at 100°C, (b) definition of ΔR_f , t_f and t_c . Demetriou C., Nestoros M. and Christofides C. Appl. Phys. A 2008; 92 (3), 651-658

The equilibrium constants K_{mol} and K_{diss} for the cases of molecular adsorption and dissociative adsorption respectively are:

$$K_{mol} = \frac{k_a}{k_d} \quad (a)$$

$$K_{diss} = \sqrt{\frac{k_a}{k_d}} = \sqrt{K_{mol}} \quad (b) \quad (18)$$

4.1.3. Experimental results and discussion

The sensor was exposed to various concentrations of hydrogen in nitrogen environment, and afterwards only to nitrogen gas. One can observe a quick rise upon the introduction of H_2 followed by a slower one up to the saturation point. The saturation point occurs at longer times with increasing concentrations of hydrogen (Figure 3(a)). Once the nitrogen gas was introduced following hydrogen saturation in the chamber, the PMTR signal decreased and returned to equilibrium. It is important to note that the photothermal signal decreases faster at low hydrogen concentration. In addition, according to Figure 3(a), the PMTR signal change is higher for larger amounts of hydrogen in the chamber. This is consistent with eqs. (18a) and (18b). The experimental data were fitted using the Langmuirian model defined from eqs. (12)-(14) as well as eqs. (15) and (16). As result the rate constants of adsorption k_a , desorption k_d were extracted. The equilibrium constant K_{diss} and the surface coverage at saturation θ_s were then calculated. As shown in Figure 4(a) and (b) the experimental results are following the model describing molecular adsorption in the early part of the signal rise, while at later times there is a significant deviation. As it can be seen from Figure 4(c) and (d), the theoretical model describing dissociative adsorption is in very good agreement with the experimental data, indicating that the process of hydrogen adsorption on palladium is dissociative as mentioned in bibliography [21,23]. The extracted values of k_a and k_d are presented in Tables 1 and 2 (Table 2 for $k_d = 0$). One can observe a decrease of the values of k_a and k_d with increasing hydrogen concentration. Furthermore the rate constant of desorption k_d is several orders of magnitude smaller than the k_a constant which supports the decision of ignoring the desorption process for both types of molecular and dissociative adsorptions. The decrease of the adsorption rate constant k_a as the hydrogen partial pressure increases could be the result of site to site interactions upon high coverage. For this reason the saturation point occurs at longer times for higher hydrogen concentration.

P (ppb)	k_a ($Pa^{-1}s^{-1}$)	$\sigma(k_a)$ ($Pa^{-1}s^{-1}$)	k_d (s^{-1})	$\sigma(k_d)$ (s^{-1})	α (mV)	$\sigma(\alpha)$ (mV)
25	3.457	± 0.555	1.382×10^{-3}	$\pm 1.260 \times 10^{-3}$	1.781	± 0.187
50	2.220	± 0.148	1.281×10^{-3}	$\pm 0.312 \times 10^{-3}$	2.702	± 0.094
100	0.717	± 0.011	5.930×10^{-4}	$\pm 0.342 \times 10^{-4}$	4.596	± 0.033
150	0.448	± 0.004	5.799×10^{-7}	$\pm 55.030 \times 10^{-7}$	5.186	± 0.002

Table 1. Parameters obtained by fitting the dissociative adsorption model

Using the values of k_a and k_d which were obtained by fitting to the dissociative adsorption equation, the equilibrium constant K_{diss} and the surface coverage at saturation θ_{diss} were

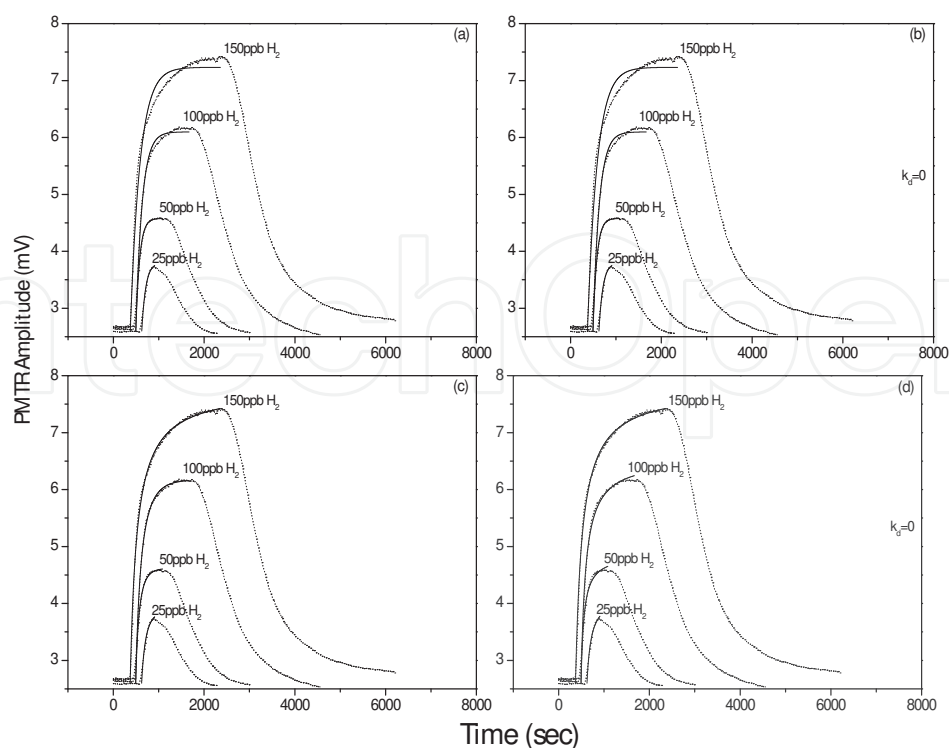


Figure 4. Molecular adsorption: (a) and (b), dissociative adsorption: (c) and (d), and fits with solid line. Demetriou C., Nestoros M. and Christofides C. Appl. Phys. A 2008; 92 (3), 651-658

calculated. The calculated values of K_{diss} are presented in Table 3 and are of the same order of magnitude for the different values of hydrogen partial pressure. At 150 ppb the equilibrium constant K_{diss} is an order of magnitude greater than the ones calculated for the lower concentrations. This is due to the small value of the rate constant of desorption k_d at 150 ppb.

P (ppb)	k_a (Pa ⁻¹ s ⁻¹)	Δk_a (Pa ⁻¹ s ⁻¹)	α (mV)	$\sigma(\alpha)$ (mV)	θ_f (%)
25	4.221	±0.202	1.568	±0.028	70.16
50	3.200	±0.086	2.269	±0.013	83.75
100	0.995	±0.010	3.956	±0.007	88.48
150	0.449	±0.002	5.185	±0.005	90.64

Table 2. Parameters obtained by fitting dissociative adsorption model and neglecting any desorption process

The calculated value of the equilibrium constant has also large errors. This is due to the large statistical errors of the rate constants of adsorption and mainly of the rate constants of desorption as shown in Table 1. Since the mechanism of desorption is negligible during adsorption process, it is not possible to determine the rate constant of desorption and consequently the equilibrium constant, taking into account only the adsorption process. The values

P (ppb)	θ_f (%)	$K_{\text{diss}}(\text{Pa}^{-1/2})$	$\sigma(K_{\text{diss}}) (\text{Pa}^{-1/2})$	θ_s (%)
25	61.77	50.016	± 23.150	71.44
50	70.33	41.628	± 5.256	74.64
100	76.15	34.778	± 1.038	77.67
150	90.62	879.380	± 4170.413	99.08

Table 3. Calculations of K_{diss} and θ_s using the values of k_a and k_d from Table 1

of the palladium surface coverage θ_f at time t_f presented in Tables 2 and 3 are larger for higher hydrogen concentrations. The values of θ_f were calculated using the following relationship $\theta_f = \Delta \zeta_f / \alpha$. The quantity α was obtained by fitting experimental data to theory and $\Delta \zeta_f$.

A similar process was followed in order to study the desorption process (nitrogen enters the chamber). The equations were solved once more letting the partial pressure to be zero. The solutions for molecular and dissociative adsorption are given by eqs. (19a) and (19b), respectively.

$$\theta_p(t) = \theta_f \exp[-k_d(t - t_f)] \quad (\text{a})$$

$$\theta_p(t) = \frac{\theta_f}{1 + k_d \theta_f(t - t_f)} \quad (\text{b}) \quad (19)$$

In Figure 5 (a) and (b) the experimental data are fitted using the above equations with the theory of molecular and dissociative desorption respectively. Note that by fitting the equation of molecular desorption to the experimental data one gets much better results. Table 4 presents the resulting values of the rate constant of desorption k_d for the different hydrogen concentrations. As shown in Table 4, the rate constant k_d is of the same order of magnitude and varies slightly with hydrogen concentration. This contradicts the fact that the recovery time of the PMTR signal is larger for higher hydrogen concentrations, as will be shown later. Using the data of Figure 3(a), the response time t_s and the recovery time t_c of the hydrogen sensor were determined. The response time is defined as the time needed for the PMTR signal to reach saturation, i.e. for the system to reach equilibrium. The time needed for the system to recover from saturation to its initial state is defined as the recovery time.

P (ppb)	$k_d (\text{s}^{-1})$	$\sigma k_d (\text{s}^{-1})$
25	2.592×10^{-3}	$\pm 0.012 \times 10^{-3}$
50	1.887×10^{-3}	$\pm 0.007 \times 10^{-3}$
100	1.475×10^{-3}	$\pm 0.002 \times 10^{-3}$
150	1.463×10^{-3}	$\pm 0.002 \times 10^{-3}$

Table 4. Desorption rate constants

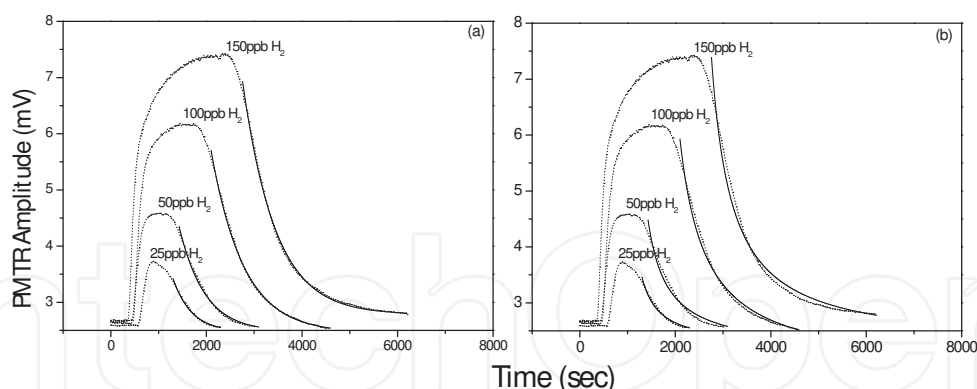


Figure 5. Molecular desorption (a) and dissociative desorption (b), data and fit. Demetriou C., Nestoros M. and Christofides C. *Appl. Phys. A* 2008; 92 (3), 651-658

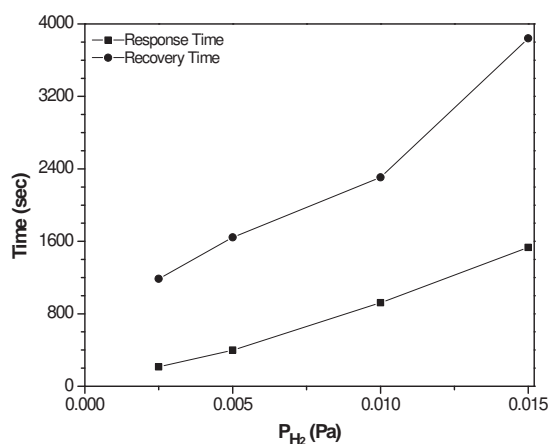


Figure 6. Response (lower curve) and recovery (upper) times versus hydrogen partial pressure. Demetriou C., Nestoros M. and Christofides C. *Appl. Phys. A* 2008; 92 (3), 651-658

As shown in Figure 6, the response and the recovery times increase by introducing larger concentrations of hydrogen gas into the cell. As mentioned before, the increase of t_c for higher hydrogen partial pressure contradicts the results that occur by studying the time progress of the desorption process. The apparent contradiction of recovery time increase for higher partial pressures of hydrogen may be due to hydrogen bonding between adjacent adsorbate protons or even molecules (i.e. before dissociation occurs on the Pd surface). This would effectively account for the dependence of the rate constant on pressure and its decrease with increasing coverage. Moreover, it should be pointed out that the response and the recovery times are determined by the experimental conditions. Previous experimental work has shown that the sensor's response time is decreased if the hydrogen gas flow rate into the cell is increased. In addition, it has been proved that by introducing into the cell an inert gas, in order to remove hydrogen, the recovery time decreases drastically. In the experiment presented [18] in this chapter nitrogen gas was introduced into the measurement cell. The presence of nitrogen gas

in the cell helps the hydrogen desorption process in the following mechanism: At saturation point, the hydrogen concentration in gas phase (above the palladium film) is in balance with the adsorbed hydrogen concentration. When nitrogen is introduced into the cell, it drifts the hydrogen molecules which are in gas phase, thus disturbing the system's equilibrium. In order for the system establish its balance again, hydrogen is desorbed from the palladium film and returns to gas phase. For bigger gas flow rates in the chamber the recovery of the signal from the saturation point to the initial value occurs faster. The measurements presented in Figure 3(a) were carried out under constant flow rate of gases of 150 mL/min, hence the comparison between the resulted values of t_s and t_c is possible. It should be noted that the sorption rate constants k_a and k_d , have an exponential dependence on the absolute temperature T of the form $K \sim \exp(-E_A/R T)$ where E_A is the activation energy of adsorption (E_A^{ads}) or desorption (E_A^{des}). Therefore, at higher temperatures the adsorption and desorption rate constants are increased resulting to the reduction of the response and the recovery time. It is also important to note that the Pd-H (hydride) phase transition does not occur in this system. According to [24] for a 6.5 nm palladium film, which is close to the thickness of our film (6 nm) no transition has been observed for hydrogen concentrations lower to 1%. Thus, for hydrogen concentrations of a few ppb no phase transition can occur. The possibility of a Pd-H (hydride) phase transition is considered to be very small, since the hydrogen concentrations used are extremely low and the sample thickness is very small. Some previous work done [25,26] from other researchers investigating the above phase transition does not present data for palladium films with thickness below 6 nm.

4.2. Photothermal radiometry applied on polymer-nanotube blends

4.2.1. Introduction

Polymer-based materials with electro-active functionalities have attracted significant attention due to their potential technological applications in many fields ranging from optoelectronics (solar cells, LED's, sensors, thin film transistors), to informatics (optical data storage) and biomaterials (artificial muscles). Carbazole-containing polymers present a lot of interest due to their potential applications as photoconductors, solar cells, gas sensors and photorefractive or charge transporting materials [27-28]. Carbazolyl groups easily form relatively stable radical cations (holes), present comparatively high charge carrier mobility and exhibit high thermal and photochemical stability. Furthermore polymers with fluorinated groups present either in the main backbone or in the side chain, exhibit some outstanding properties, including high thermal stability, chemical inertness, low dielectric constant and dissipation factors, low water absorptivity, and good resistance to surface properties [29-30]. In addition the ability of these materials to stabilize carbon nanotubes in organic solvents via non-covalent (physical) adsorption, renders them promising for use in carbon nanotube (CNT)-based nanotechnology. In general the introduction of carbon nanotubes (CNT's) enhances the mechanical stability of polymers and modifies the thermal and optoelectronic properties since CNT's act as electron acceptors. Although the mechanical properties of composites improve with the addition of CNT's, the electronic behavior is often optimum at low concentrations of nanotubes usually close to the percolation threshold.

Much work has been done concerning the modelling and measurement of the mechanical, optical and electrical properties of the composites while less work has been done concerning the evaluation of their thermal properties. Nevertheless the knowledge of thermal properties (thermal effusivity and conductivity) is of great interest in applications (biological implants, electronic packaging) where thermal management is important or in thermoelectric power applications. The polymers have low values of thermal conductivity (a representative value is 0.2 W/m K) which depends on the degree of crystallinity of the polymer among other factors. Since carbon nanotubes (CNT's) single wall (SWCNT's) or multi-wall (MWCNT's) have very high thermal conductivity (2800-6000 W/m K) it is expected that their introduction to the polymer will greatly enhance the effective thermal conductivity. Although there is a large scatter in the experimental results [31] (some of them are contradictory) the polymer-CNT composites still present quite low values of thermal conductivity. This is attributed to the phonon mismatch at the polymer/CNT interface resulting in high interface thermal resistance. The work [32] described in this paragraph employs a non-contact and non-destructive technique, photothermal radiometry (PTR) to study heat transport in a novel type of polymer loaded with SWCNT's at various concentrations. A two layer photothermal model is used to analyze thermal transport in the composite film which is deposited on quartz substrate. Furthermore, optical measurements are used to extract the absorption coefficient of the thin films at the excitation beam wavelength and hence eliminate one of the unknown parameters in the theoretical model. A simultaneous fitting of the experimental signal amplitude and phase is compared to the calculated signal in order to extract the thermal properties of the thin composite films.

4.2.2. Materials

A series of well-defined diblock copolymers consisting of 2-(N-carbazolyl)ethyl methacrylate (CbzEMA) and 2,2,3,3,4,4,4-heptafluorobutyl methacrylate (HFBMA) (CbzEMA_x-b-HFBMA_y) was synthesized by Reversible Addition-Fragmentation chain Transfer (RAFT) controlled radical polymerization [33]. The RAFT process allows for the preparation of functional polymeric materials characterized by pre-determined molecular weights, narrow molecular weight distributions and pre-defined architectures [34,35]. The polymer films were generated by spin coating on 0.9 cm x 0.9 cm quartz substrates of a dilute THF solution of CbzEMA₅₂-b-HFBMA₆₉ and SWCNTs at room temperature. The single wall carbon nanotubes (SWCNT's) used, where 4-5nm (diameter) x 500-1500nm (length) bundles, with 80-90 % carbonaceous purity from Sigma-Aldrich. The first series of samples consisted of three samples (A1,A2,A3) with varying thicknesses and constant % weight of SWCNT's. The thickness of the A series samples measured by a mechanical profilometer varied in a big extend across the surface of the sample. Later on a second series of samples (B0,B1,B2,B3) with different % weight of SWCNT's was fabricated. The spin coater angular velocity was increased at 100 rev/s in order to achieve better thickness homogeneity across the sample, something which was verified by the profilometer measurements. The thickness (with a tolerance of 10 nm) and % weight of SWCNT's are shown in Table 5. The PTR experimental setup was described earlier. The excitation beam (512 nm) with incident power of 45 mW

and dimensions of approximately 2mm illuminated almost at normal incidence the center of the sample surface (composite film). As the modulation frequency was varied in the 10^2 - 10^5 Hz the signal amplitude and phase was recorded. The reproducibility of the PTR signal measurements was verified within less than 1%. In order to calculate the instrumental transfer function with which we have to correct the experimental data a frequency scan of a thick and opaque sample (steel disc) was performed.

sample	film thickness	SWCNT % weight
A1	4,62 μm	4.11
A2	6,16 μm	4.11
A3	8 μm	4.11
B0	35 nm	0
B1	30 nm	1.64
B2	40 nm	4.76
B3	62 nm	9.09

Table 5. Sample characteristics

4.2.3. Two layer photothermal model and simulations

A two layer model was developed in order to simulate the ac temperature field in the samples.

$$\frac{d^2\Delta T_f(z,\omega)}{dz^2} - \sigma_{T,f}^2 \cdot \Delta T_f(z,\omega) = -\frac{\alpha_f \cdot I_0 \cdot (1-R) \cdot e^{-\alpha_f \cdot z}}{\kappa_f} \text{ for } 0 \leq z \leq l \quad (20)$$

$$\frac{d^2\Delta T_s(z,\omega)}{dz^2} - \sigma_{T,s}^2 \cdot \Delta T_s(z,\omega) = -\frac{\alpha_s \cdot I_0 \cdot (1-R_2) \cdot e^{-\alpha_s \cdot (z-d)}}{\kappa_s} \text{ for } l \leq z \leq d+l \quad (21)$$

The illuminated surface of the polymer-nanotube blend is at $z=0$ while the interface between the blend and the substrate at $z=l$. The rear surface of the quartz glass is at $z=l+d$. The ac temperature ΔT is a function of depth z , measured from the surface of the sample and the angular modulation frequency $\omega=2\pi f$. The subscripts s and f stand for the film and substrate respectively. Using the boundary conditions below, concerning the continuity of heat flux and temperature at the interfaces, the solutions for $\Delta T(z)$ in the film and substrate can be evaluated at different values of the modulation frequency.

$$\begin{aligned}
 & -[-\kappa_f \frac{dT_f}{dz} \Big|_{z=0}] = 0 \\
 & (-\kappa_s \frac{dT_s}{dz} \Big|_{z=l}) - (-\kappa_f \frac{dT_f}{dz} \Big|_{z=l}) = 0 \\
 & T_f(z=l) = T_s(z=l) \\
 & -(-\kappa_s \frac{dT_s}{dz} \Big|_{z=l+d}) = 0
 \end{aligned} \tag{22}$$

The modulated blackbody radiation emission S_{PTR} of the sample is proportional to the weighted depth integral of the temperature field in the sample and it can be separated in two terms, the contribution of the composite film and the contribution of the substrate, as presented in eq. (23) [17] below. The weighting is related to the infrared absorption coefficient β_{ir} of the sample over the infrared detection range (2-12 μm).

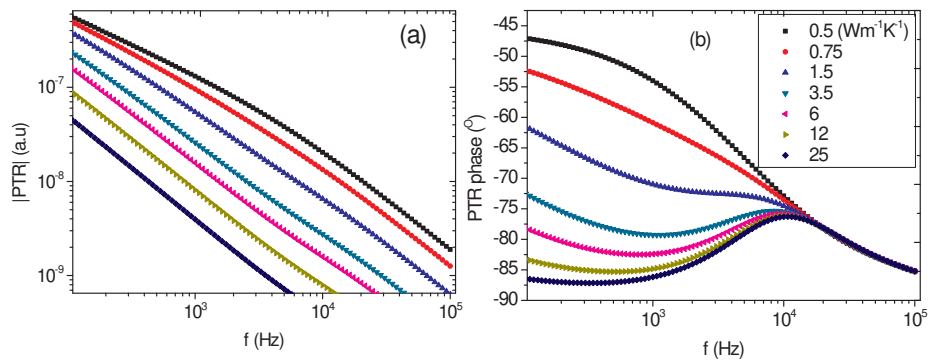


Figure 7. Dependence of photothermal signal amplitude (a) and phase (b) on the thermal conductivity (κ_f) of the film

$$S_{PTR}(\omega) \propto [\beta_{ir,f} \cdot \int_0^l \Delta T_f(z, \omega) \cdot \exp(-\beta_{ir,f} \cdot z) \cdot dz + \beta_{ir,s} \cdot \int_l^{l+d} \Delta T_s(z, \omega) \cdot \exp(-\beta_{ir,s} \cdot z) \cdot dz] \tag{23}$$

A series of simulations was performed in order to examine the influence of the film properties (absorption coefficient α , thickness, thermal conductivity and diffusivity) on the signal amplitude and phase.

The values of the optical and thermal properties of the quartz substrate used in the simulations and calculations used for fitting the theoretical results to the experimental data are: $D_s=1.4 \times 10^{-6} \text{ m}^2/\text{s}$, $\kappa_s=1.5 \times 10^{-6} \text{ W}/(\text{m K})$, $\alpha_s=30 \text{ m}^{-1}$, $\beta_{irs}=1 \times 10^7 \text{ m}^{-1}$. The thermal and properties of the quartz substrate were taken from literature while the absorption coefficient at the excitation beam was calculated from the transmission measurements. The IR absorption coefficient of the quartz substrate was taken to be practically infinite. This simplification was backed from the experiment since the PTR signal was dropping from a high value (mV) to practically noise

level when the sample orientation was reversed (beam entering the sample from the quartz substrate and then meeting the thin film). This means that the quartz substrate is opaque to the IR emission of the polymer-nanotube blend film. In addition the substrate was assumed to be transparent at the excitation beam wavelength 512 nm). Concerning the thermal properties of the composite film typical values for polymers were used for the simulations, as well as for starting values of the fitting process. The simulations show that the contribution of the quartz substrate to the overall PTR signal (second term of eq.(23)) can be ignored since the quartz substrate has a very low absorption coefficient at the excitation wavelength. Nevertheless the substrate presence in the theoretical model is necessary since it defines the correct boundary conditions at the interface. The effect of thermal conductivity on the PTR signal as function of modulation frequency is shown in Figure 7. An increase of the thermal conductivity of the film allows the generated heat to diffuse away more efficiently and hence the PTR signal amplitude decreases as the temperature field in the film weakens. The signal phase in the low frequency regime reduces with the increase of thermal conductivity, leading to the formation of an extremum at a frequency defined by the thermal diffusivity of the film.

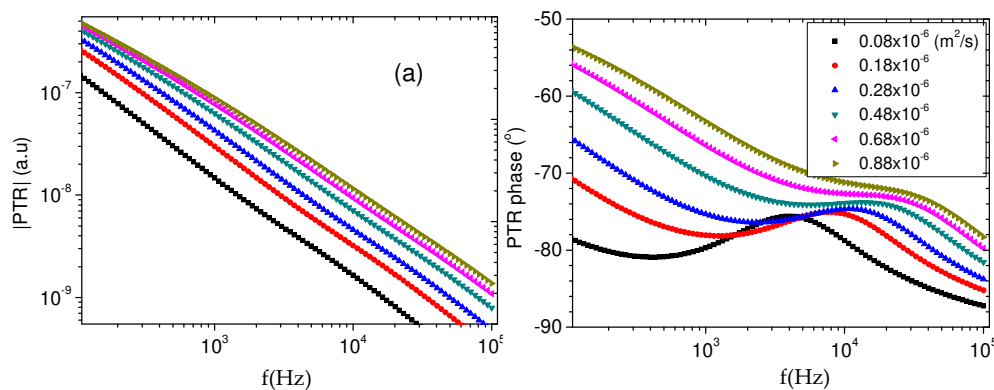


Figure 8. Dependence of photothermal signal amplitude (a) and phase (b) on the thermal diffusivity (D_t) of the film

An increase in thermal diffusivity results in an increase of the thermal diffusion length causing the shift of the phase extremum to higher modulation frequencies as seen in Figure 8, as well as an overall increase of the signal phase. The signal amplitude increases with increasing thermal diffusivity although at a first sight one would expect the opposite since high values of thermal diffusivity would mean that heat is carried out faster from the region generated. One should not forget though that the modulated IR emission of the sample is proportional to the integral of the temperature field over the thickness of the sample. Since a higher diffusivity results in a longer thermal diffusion length a thicker part of the sample will contribute to the IR emission leading to stronger signal amplitude.

A series of transmission and reflection measurements was performed in the 200 nm -3000 nm in order to help evaluate the absorption coefficient of the samples and reveal its dependence on the SWCNT content. Although the thicknesses of the samples are quite different the optical transmission measurements presented in Figure 9(a) indicate a decrease of transmission with the increase of concentration of SWCNT's. In addition it is clear that the polymers absorb

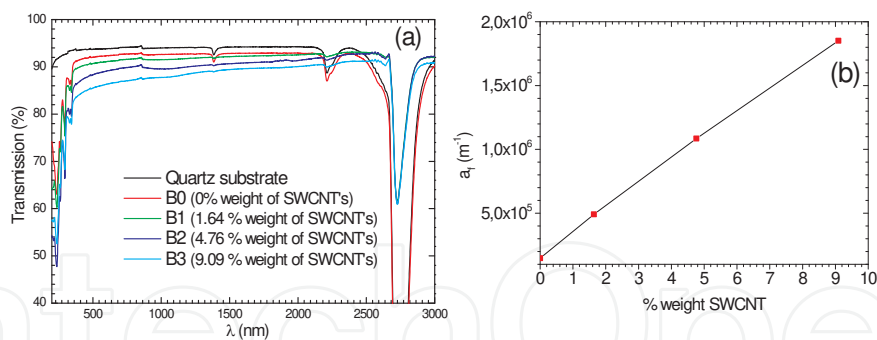


Figure 9. Transmission measurements (a) and calculated value of absorption coefficient (b) at excitation wavelength as a function of SWCNT concentration.

significantly in the UV range. The transmission deep in the 2650 nm-2900 nm is associated with the OH- bonds. The optical absorption coefficient, presented in Figure 9(b), at the excitation beam wavelength (512 nm) was calculated from the transmission and reflection spectra of the samples. Since the thickness tolerance was 10 nm the samples were assumed to have an average thickness of 42 nm. The PTR signal amplitude and phase, for A series samples, as a function of modulation frequency are shown in Figure 10. In the low frequency (<10³ Hz) range the signal amplitude differentiates well for the three samples. Since the % weight of SWCNTs's is the same for the three samples one can assume that the optical and thermal properties of the films should be very similar, ignoring non-homogeneities due to the fabrication process, hence the signal differences should be attributed to the composite film thickness variation. More specifically the signal amplitude decreases as the composite film thickness increases.

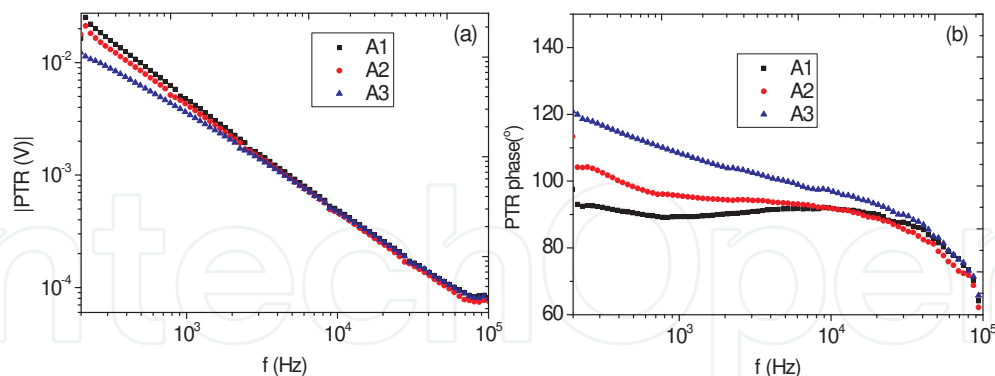


Figure 10. Experimental PTR signal amplitude (a) and phase (b) for the A series of samples

The phase channel of the signal (Figure 10(b)) can differentiate between the three samples up to a higher frequency (10⁴ Hz) range and is increasing and changing slope as the composite film thickness is increasing. The decrease of the signal amplitude has to do with the fact that the contribution of the film to the signal depends on the IR emission of the film, which is proportional to the integral of the temperature field over the thickness of the sample multiplied by the factor $\exp(-\beta_{ir} \cdot z)$ which results in a lower signal for thicker films. The extraction of the

optical and thermal properties for the composite films was accomplished by comparing (fitting) the theoretical signal to the experimental data, with the aid of a MATLAB code.

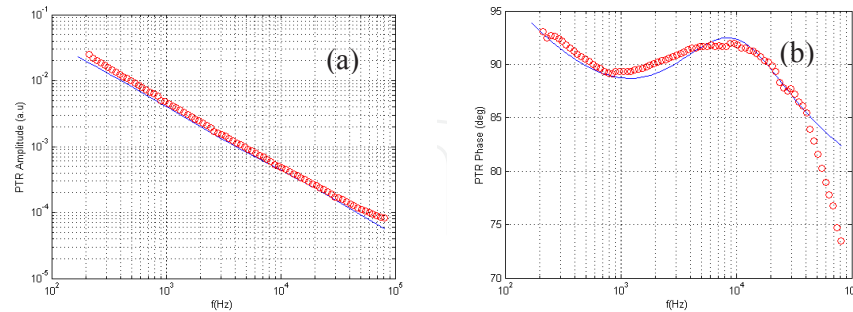


Figure 11. Theoretical signal amplitude (a) and phase (b) fit (solid lines) to the experimental signal amplitude and phase for sample A1

	A1	A2	A3
D (m ² /s)	0.19x10 ⁻⁶	0.33x10 ⁻⁶	0.59x10 ⁻⁶
κ (W/m K)	2.8	1.45	0.98
β _{ir} (m ⁻¹)	4.4x10 ⁵	4.7x10 ⁵	4.7x10 ⁵
α (m ⁻¹)	1.4x10 ⁶	1.4x10 ⁶	1.4x10 ⁶

Table 6. Extracted thermal and optical parameters for the A series samples

Both channels of experimental information i.e signal amplitude and signal phase were used in order to achieve higher accuracy. The fitting results for samples A1, A2 are shown in Figures 11 and 12 respectively while the extracted values of the thermal and optical properties of the samples are tabulated in Table 6. The theoretical curves fit quite well the experimental data, except at the edges of the frequency spectrum. This discrepancy could be due to the simplified theoretical model which ignores multiple reflections in the thin film. According to Arjona et.al [36] this is more significant for phase channel in the higher modulation frequencies while for the amplitude channel is more significant for the lower modulation frequencies. The calculated thermal parameters are within the range of values reported in the literature [30] for polymer carbon-nanotube composites. The second series (B series) of samples consists of very thin composite layers (nm range) and is more interesting since in this group we have a variation of the concentration of SWCNT's. The increase of the experimental signal amplitude among the B series samples as observed in Figure 13 could be attributed to the increased optical absorption coefficient and thermal conductivity as a function of the % weight of SWCNT's which increases from B1 to B3. The samples of B series have different concentration of SWCNTS's ranging from 0-9 % weight. Due to the increase of the angular speed of the spin coater the thicknesses of the films were now in the nm range and are actually very similar within the experimental tolerance which is 10 nm. The observed differences have then to be attributed to the change of the optical

absorption coefficient and the thermophysical parameters (thermal conductivity and diffusivity) due to the variation of the concentration of the CNT's. Nevertheless the fact that the relative uncertainty in the film thickness is quite high creates an additional obstacle for the fitting process.

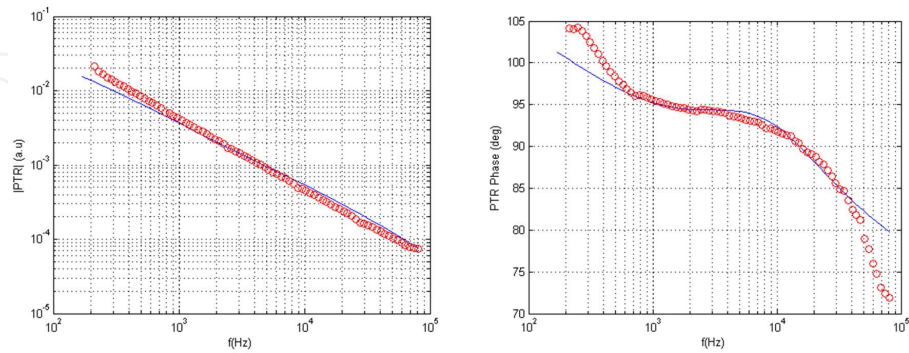


Figure 12. Theoretical signal amplitude (a) and phase (b) fit (solid lines) to the experimental signal amplitude and phase for sample A

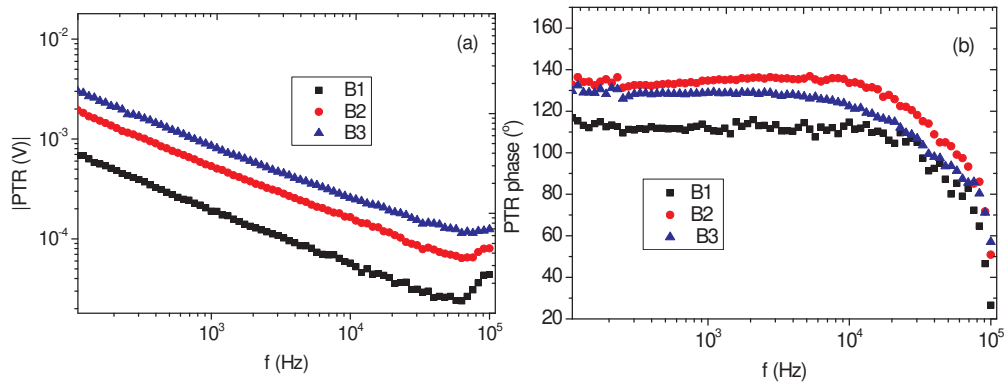


Figure 13. Experimental PTR signal amplitude (a) and phase (b) for the B series of samples

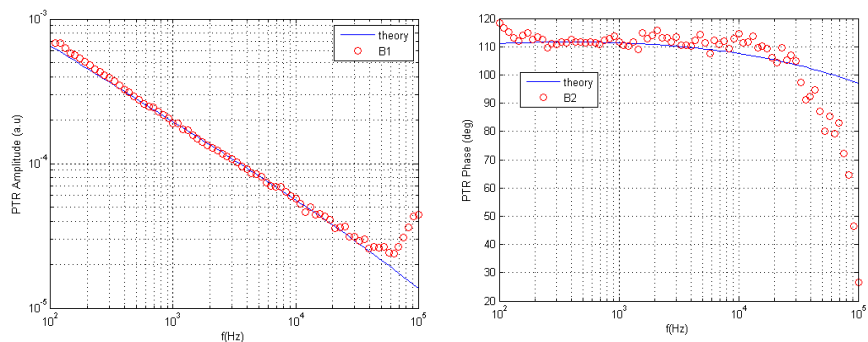


Figure 14. Theoretical signal amplitude (a) and phase (b) fit (solid lines) to the experimental signal amplitude and phase for sample B1

In general an increase in thermal conductivity which is expected with the addition of CNT's should be accompanied with a reduction of the signal amplitude in contrast with the experimental results shown in Figure 13. Nevertheless the simulations indicate that for thinner (~ 20 nm-B series) the amplitude variation with the increase of thermal conductivity is much smaller as compared to the case of thicker films ($\sim \mu\text{m}$ range-A series). In addition the simulations show that the signal amplitude is affected more by the optical absorption coefficient. This means that the small decrease in amplitude due to the increase of thermal conductivity is masked by a much bigger amplitude increase due to the increase of the absorption coefficient at the excitation wavelength. In the case of sample B1 the fitted values were $\kappa_f=2.0$ W/mK and $D_f=1.06 \times 10^{-7}$ m²/s. The fitting for samples B1 and B2 was not attempted due to the high uncertainty in the film thickness which was about the same size as the measured value of the thickness.

5. Conclusion

In this chapter we introduced the physics of thermal and electronic waves that underpin photothermal phenomena and described two basic photothermal techniques, namely Photo-Modulated Thermoreflectance (PMTR) and Photothermal Radiometry (PTR). The abilities of these experimental techniques were explored in the study of thin metal film-gas interaction kinetics and the optical and thermal characterization of composite materials.

In the first application it was verified that that hydrogen adsorbs to palladium dissociatively while desorption is characterized by a molecular reaction. As a consequence of the high sensitivity of the PMTR sensor, the determination of the rate constants of adsorption k_a and desorption k_d for very small H₂ concentrations was possible. In addition the analysis of the time evolution of the PMTR signal showed that the values of k_d were several orders of magnitude smaller than the ones resulting for the rate constant of adsorption k_a . Thus, in order to study the adsorption process, the competitive mechanism of desorption should not be taken into account. For the adsorption mechanism it was observed that the resulting values of the adsorption rate constant k_a decrease with the increase of H₂ concentration. These results also justify the increase of the sensor's response time for larger H₂ concentrations.

In the second application it was shown that Photothermal Radiometry (PTR) is able to characterize composite materials like polymer-carbon nanotube blends. The photothermal signal (amplitude and phase) is very sensitive to the change of SWCNT's concentration as well as to the polymer film thickness. With the aid of a two layer photothermal model it was possible to extract thermal and optical properties of the composite materials.

Acknowledgements

I gratefully acknowledge the contribution and collaboration of Prof. C. Christofides and Prof. A. Othonos, directors of the Photonics and Optoelectronics Laboratory at the University of

Cyprus where the photothermal experiments took place. I would like to express my thanks to Dr. T. Krasia and Ms. I. Savva from the Department of Mechanical and Manufacturing Engineering, University of Cyprus for the fabrication of the polymer-nanotube blend samples as well as to Dr. N. C. Papanicolaou from the Department of Computer Science, University of Nicosia for his contribution in the modelling and simulations of the photothermal response of the polymer-carbon nanotube blends.

Author details

Marios Nestoros

Department of Electrical & Computer Engineering, University of Nicosia, Nicosia, Cyprus

References

- [1] Mandelis A. Diffusion-Wave Fields, Mathematical Methods and Green Functions. New York: Springer; 2001.
- [2] Fournier D., Boccara C., Skumanich A. and Amer N.M. Photothermal investigation of transport in semiconductors: Theory and experiment. *Journal of Applied Physics* 1986; 59(3) 787-795.
- [3] Ikari T., Salnick A. and Mandelis A. Theoretical and experimental aspects of three-dimensional infrared photothermal radiometry of semiconductors. *Journal of Applied Physics* 1999; 85(10), 7392 – 7397.
- [4] Rosengwaig A., Opsal J., Smith W. L. and Willenborg D. L. Detection of thermal waves through optical reflectance. *Applied Physics Letters* 1985;46(11) <http://dx.doi.org/10.1063/1.95794>.
- [5] Wurm S., Alpern P., Savignac D and Kakoschke R. Modulated optical reflectance measurements on amorphous silicon layers and detection of residual defects. *Applied Physics A* 1988; 47(2) 147-155.
- [6] Christofides C. Photomodulated Thermoreflectance of Implanted Wafers. In Christofides C., Ghibaudo G. (eds.) *Effect of Disorder and Defects in Ion-Implanted Semiconductors: Optical and Photothermal Characterization, Semiconductors and Semimetals*, Vol. 46. New York: Academic Press; 1997. p 115-147.
- [7] Fotsing J. L. N., Hoffmeyer M., Chotikaprakhan S., Dietzel D., Pelzl J., Bein B. K., Cerqueira F., Macedo F., and Ferreira J. A. Laser modulated optical reflectance of thin semiconductor films on glass. *Review of Scientific Instruments* 2003;74(1) 873-876.

- [8] Lavega-Sanchez A., Salazar A., Ocariz A., Pottier L., Gomez E., Villar L.M, Macho E., Thermal diffusivity measurements in porous ceramics by photothermal methods. *Applied Physics A* 1997; 65 (1) 15-22.
- [9] Schmidt A. J., Cheaito R., and Chiesa M. Characterization of thin metal films via frequency-domain thermoreflectance. *Journal of Applied Physics* 2010; 107(2), 024908.
- [10] Ikari T., Roger J. P, and Fournier D. Photothermal microscopy of silicon epitaxial layer on silicon substrate with depletion region at the interface. *Review of Scientific Instruments* 2003;74(1) 553-556.
- [11] Sheard S., Somekh M., and Hiller T. Non-contacting determination of carrier lifetime and surface recombination velocity using photothermal radiometry. *Material Science and Engineering: B* 1990; 5(2) 101-105.
- [12] Othonos A., Christofides C. and Mandelis A. Photothermal radiometric investigation of implanted silicon: The influence of dose and thermal annealing. *Applied Physics Letters* 1996; 69(6) 821-823.
- [13] Ravi J., Lu Y., Longuemart S., Paoloni S., Pfeiffer H., Thoen J., and Glorieux C. Optothermal depth profiling by neural network infrared radiometry signal recognition. *Journal of Applied Physics* 2005; 97(1) <http://dx.doi.org/10.1063/1.1821635>
- [14] Christofides C., Nestoros M. and Othonos. A Photothermal Radiometric Study of Implanted Semiconductors. In: Mandelis A. and Hess P. (eds.) *Progress in Photothermal and Photoacoustic Science and Technology, Volume IV: Semiconductors and Electronic Materials*. Bellingham; SPIE; 2000. p110-142.
- [15] Depriester M., Hus P., Delenclos S., and Sahraoui H. A. Study of thermal parameters' temperature dependence in solids using photothermal radiometry. *Review of Scientific Instruments* 2007; 78(3), 109-113.
- [16] Macedo F., Vaz1 F., Torrelli M., Faria R. T., Cavaleiro A., Barradas N. P., Alves E., Junge K. H. and Bein B. K. TiO₂ coatings with Au nanoparticles analysed by photothermal IR radiometry. *Journal of Physics D: Applied Physics* 2012; doi: 10.1088/0022-3727/45/10/105301
- [17] Hellen A., Matvienko A., Mandelis A., Finer Y., and Amaechi B. T. Optothermophysical properties of demineralized human dental enamel determined using photothermally generated diffuse photon density and thermal-wave fields. *Applied Optics* 2010;49, (36) 6938-6951.
- [18] Demetriou C., Nestoros M. and Christofides C. Photothermal hydrogen sensor: the technique, experimental process, and physicochemical analysis. *Applied Physics A* 2008; 92 (3), 651-658.
- [19] Schlappbach L., Züttel A., Gröning P., Gröning O. and Aebi P. Hydrogen for novel materials and devices. *Applied Physics A* 2001;72(2), 245-253.

- [20] Kalli K., Othonos A. and Christofides C. Characterization of reflectivity inversion, α - and β -phase transitions and nanostructure formation in hydrogen activated thin Pd films on silicon based substrates. *Journal of Applied Physics* 2002; 91(6) 3829 – 3840.
- [21] Mandelis A. and Christofides C. *Physics, Chemistry and Technology of Solid State Gas Sensor Devices*, Vol. 125 in *Chemical Analysis*. New York: Wiley Interscience; 1993.
- [22] Lundström I. Why bother about gas-sensitive field-effect devices? *Sensors and Actuators A* 1996; 56(1-2),75-82.
- [23] Lundström I., Shivaraman M.S, and Svensson C. Chemical reactions on palladium surfaces studied with Pd-MOS structures. *Surface Science* 1977;64 497-519.
- [24] Wang C., Mandelis A. and Garcia J.A. Pd/PVDF Thin Film Hydrogen Sensor System based on Photopyroelectric Purely-Thermal-Wave Interference. *Sensors Actuators B* 1999; 60 228 – 237.
- [25] Christofides C., and Mandelis, A. Operating characteristics and comparison of photopyroelectric and piezoelectric sensors for trace hydrogen gas detection. I. Development of a new photopyroelectric sensor. *Journal of Applied Physics* (1989); 66(9) 3986-3992.
- [26] Christofides C., Mandelis A., Rawski J. and Rehm S. Photopyroelectric detection of hydrogen/oxygen mixtures. *Review of Scientific Instruments* 1993; 64(12) 3563- 3571.
- [27] Gerad M., Chaubey A. and Malhotra B. Application of conducting polymers to biosensors *Biosensors & Bioelectronics* 2002; 17(5) 345–359.
- [28] Brar A. S. and Gandhi S. Microstructure determination of 9-ethyl-3-hydroxymethyl-carbazoyl acrylate/methacrylonitrile using two-dimensional NMR spectroscopy. *Journal of Molecular Structure*, 2007; 832(1-3) 26–37.
- [29] Zheng-hong L. and H. Teng-yun H. Synthesis and characterization of poly(dimethylsiloxane)-block-poly(2,2,3,3,4,4,4-heptafluorobutyl methacrylate) diblock copolymers with low surface energy prepared by atom transfer radical polymerization. *Reactive & Functional Polymers*, 2008, 68(5) 931–942.
- [30] Wang QY., Zhang QH., Zhan XL. and Chen FQ., Low Surface Energy Polymer with Fluorinated Side Group. *Progress in Chemistry* 2009; 21(10) 2183-2187.
- [31] Han Z., Fina A. Thermal conductivity of carbon nanotubes and their polymer nanocomposites: A review. *Progress in Polymer Science* 2011; 36(7) 914-944.
- [32] Nestoros M., Savva I., Krasia T., Papanicolaou N. C., Othonos A. and Christofides C. Thermal and optical characterization of methacrylate-based polymers with embedded carbon nanotubes, 9th International Conference on Nanosciences & Nanotechnologies, 3-6 July, 2012, Thessaloniki, Book of Abstracts p. 134.
- [33] Savva I., Demetriou M., Othonos. A, Turcu R., Popa A., Macavei S. and Krasia-Christoforou T. Well-defined fluoro- and carbazole-containing diblock copolymers: syn-

thesis, characterization and immobilization onto Au-coated silicon surfaces. RSC Advances 2012; 2(10) 8741-8751.

- [34] Sun G., Cheng C. and Wooley K.L. Reversible Addition-Fragmentation Chain Transfer (RAFT) Polymerization of 4-Vinylbenzaldehyde. *Macromolecules* 2007; 40(4) 793-795.
- [35] Konkolewicz D., Hawket B. S., Weale A. G., Perrier S. Raft Polymerization Kinetics: How long are the Cross-Terminating Oligomers? *Journal of Polymer Science: Part A: Polymer Chemistry* 2009; 47(14) 3455-3466.
- [36] Arjona-Zambrano M. A., Miranda-Ordonez J., Esquivel-Medina R. A, Peñuñuri F., Martinez P. and Gil-Alvarado J. J. Effect of the multiple reflections of a light beam on the thermal wave field of a sample of finite thickness. *Journal of Applied Physics* 2012; 111(9) <http://dx.doi.org/10.1063/1.4717115>

IntechOpen